Article:
Ghalambaz, M, Mehryan, SAM, Ismael, MA et al. (2019) Fluid–structure interaction of free convection in a square cavity divided by a flexible membrane and subjected to sinusoidal temperature heating. International Journal of Numerical Methods for Heat & Fluid Flow, 30 (6). pp. 2883-2911. ISSN: 0961-5539

https://doi.org/10.1108/hff-12-2018-0826

Fluid-Structure Interaction of Free Convection in a Square Cavity Divided by a Flexible Partition and Subjected to Sinusoidal Temperature Heating

S. A. M. Mehryan

Young Researchers and Elite Club, Yasooj Branch, Islamic Azad University, Yasooj, Iran. E-mail: a.mansuri1366@gmail.com

M. A. Ismael

Mechanical Engineering Department, Engineering College, University of Basrah, Basrah, Iraq. E-mail: muneerismael@yahoo.com, muneer.ismael@uobasrah.edu.iq

M. Ghalambaz*

Islamic Azad University & School of Aeronautic Science and Engineering, Beihang University, Beijing, P.R. China

Ali J. Chamkha

Mechanical Engineering Department, Prince Mohammad Bin Fahd University, Al-Khobar 31952, Saudi Arabia

Prince Sultan Endowment for Energy and Environment, Prince Mohammad Bin Fahd University, Al-Khobar 31952, Saudi Arabia, E-mail: achamkha@pmu.edu.sa

D. Wen [a,b*]

[a]School of Aeronautic Science and Engineering, Beihang University, Beijing, P.R. China

[b].School of Chemical and Process Engineering, University of Leeds, Leeds, U.K.

Emails: d.wen@buaa.edu.cn

ABSTRACT: The problem of Fluid-solid interaction (FSI) with free convection inside a periodically-heated quadrilateral regular enclosure is investigated numerically in this paper. The cavity is equally divided vertically by a thin flexible wall. The cavity is differentially heated by a sinusoidal time varying temperature on the left vertical wall while the right vertical wall is cooled isothermally. There is no thermal diffusion from the upper and lower boundaries. The finite element Galerkin technique with the aid of an arbitrary Lagrangian-Eulerian procedure is followed in the numerical procedure. The effects of four pertinent

parameters are investigated, i.e., Rayleigh number ($10^4 \le Ra \le 10^7$), elasticity modulus ($5\times10^{12} \le E_\tau \le 10^{16}$), Prandtl number ($0.7 \le Pr \le 200$) and temperature oscillation frequency ($2\pi \le f \le 240\pi$). The results have shown that there is not significant effect of the temperature frequency on the mean values of the Nusselt number and the deformation of the flexible divider. The convective heat transfer and the stretching of the thin flexible divider become higher with a fluid of a higher Prandtl number or with a partition of lower elasticity modulus.

Keywords: Fluid-structure interaction (FSI); flexible partition; sinusoidal temperature; square cavity.

Nomenclature

$\boldsymbol{d}_s$	vector of displacement
E	Young's modulus in dimensional form
E_τ	elasticity modulus in non-dimensional form
F	frequency
$\boldsymbol{F}_v$	vector of body force
$\boldsymbol{g}$	vector of gravitational acceleration
L	size of cavity
P	fluid pressure
Pr	Prandtl number
Ra	thermal Rayleigh number
t	time
T	temperature
T_p	period of oscillation
x, y	Cartesian coordinates
$\boldsymbol{u}$	vector of velocity

$\boldsymbol{w}$	velocity vector of the moving grid

Greek symbols

α	thermal diffusivity
β	volumetric thermal expansion coefficient
σ	Tensor of stress
τ	non-dimensional time
μ	dynamic viscosity
v	Poisson's ratio
ρ	density
ρ_R	density ratio of fluid to solid structure

Subscripts

av	average
c	cold temperature
f	fluid
h	hot temperature
p	partition
s	solid

Superscripts

*	indicates the dimensional parameters

1. Introduction

Many engineering applications have promoted the problem of natural convection inside enclosures, which has attracted intensive research interest. For example, Emery [1] presented experimental and numerical results for natural convection amongst vertical sheets for very wide range of Prandtl numbers (1 to 20000). de Vahl Davis [2] performed a benchmark numerical solution of the equations governing 2D free convection in a square enclosure filled with air. Patterson and Armfield [3] presented numerical analysis and

experimental data for 2D unsteady free convection induced by an instantly differentially-heated square cavity. They focused on the instability of travelling wave and its effect on the thermal boundary layer close to the vertical wall(s)**.** Kelkar and Patankar [4] illustrated that existence of the partition located in cavities were almost unimportant when such partition did not cover more than the enclosure mid-height. Ciofalo and Karayiannis [5] studied, numerically, the efficiency of partitions extending from the vertical/horizontal bounds on the rate of heat exchange in a rectangular cavity. They reported that the effect of the partition was completely dependent on Rayleigh number and the cavity aspect ratio. Fusegi et al. [6] conducted a study on three-dimensional steady-state free convection in a cubical cavity. They demonstrated a small (in magnitude) transverse z- velocity component**.** Markatos and Pericleous [7] presented a numerical solution for buoyancy-driven laminar and turbulent convection (Rayleigh = 10^3 to 10^{16}) in a square cavity. Kuyper et al. [8] carried out a numerical simulation dealing with laminar and turbulent (Rayleigh = 10^4 to 10^{10}) free convection in an inclined square. They found a solution hysteresis at a transition of flow pattern. Barakos et al. [9] utilized the control volume method to simulate the laminar and turbulent free convection in a square enclosure. They demonstrated that the standard k-ϵ model was constrained to logarithmic wall functions. Baïri et al. [10] reviewed the applications of free convection in enclosures with explaining the different solutions to treat natural convection phenomena. They also explained the effects of inclination, geometry, aspect ratio, working fluid and the flow regimes on the features of flow and temperature fields. However, the classical and review works of [1-10] demonstrated the importance of natural convection in enclosures.

Moreover, the natural convection in buildings and the insulation of heat storage systems can be simulated by cavities divided by impermeable dividers [11-13], which has extensively studied. Different characteristics of free convection heat transfer were studied to improve or control the heat transfer process in homogeneous cavities [14], [15]; and in partitioned cavities such as a diagonally-divided square cavity [16]; a cavity with an off-center partition [17]; a cavity with multiple vertical partitions [18]; a vertically-divided cavity [19]; and divided cavities with various thermal boundary conditions [19]; a partitioned cavity subject to a uniform heat flux [20] and partitioned cavities with various thermal boundary conditions [21-23].

Flow through devices incorporated with diaphragm like pump and sensors, flow through flexible conduits, and reciprocating pistons or fluid splashing in containers of flexible wall [24] are deformable-domain problems. The most efficient and robust numerical method developed in such problems is the Arbitrary Lagrangian-Eulerian method (ALE) [25]. Fu and Huang [26] straddled this numerical approach to study the free convection in a vertical channel containing a vibrated surface. They found lesser convection effect compared with stationary surface. Lee *et al*. [27] investigated the impact of elasticity property of flapping wings on the thrust generation. They indicated a major role of the modulus of elasticity on the drag exerted by flow. Kalmbach and Breuer [28] have provided reference experimental data regarding FSI benchmark case under turbulent flow conditions. Their structure consisted of a rigid cylinder tailed with a para-rubber sheet acting as a splitter. At the end of the para-rubber sheet, a mass was attached to reduce flutter effect. They found the flexible splitter reduced the drag of flow compared with rigid splitter. De Nayer and Breuer [29] utilized the FSI experiments of [28] along with the large-eddy simulation to show that the modulus of elasticity of rubber had essential effect on the FSI phenomenon. Ghalambaz *et al*. [30] employed the ALE approach to study the effect of a horizontal oscillating fin on the convective heat exchange in a differentially heated cavity. The oscillating fashion of the fin did not overcome its drag action. Therefore, they recognized the deterioration of the heat exchange despite the mixing effect introduced by the fin.

Very recently, Jamesahar *et al.* [31] and Mehryan *et al.* [32] considered the free convection in cavities subdivide by flexible membrane by studying the fluid-solid interaction between the free convection and the membrane. Jamesahar *et al.* [31] showed that the reformable cavities affected the rate of heat exchange compared with a rigid partition. The results of Mehryan *et al*. [32] confirmed that the shape of a very thin flexible partition (membrane) was significantly influenced by the fluid interaction with the solid. Both studies of Jamesahar *et al.* [31] and Mehryan *et al.* [32] concluded that the deformable membrane could influence the flow and heat patterns in the cavity. Therefore, both of the fluid and structure were coupled and should be solved simultaneously. In both studies ([31] and [32]) the main cavities were differentially heated. However, in many real applications, imposing the perfectly constant wall temperature is hard to be attained. Practically, the wall

temperature fluctuates about a range of temperature with a periodic fluctuation frequency. By careful study of the physics of a cavity containing a flexible partition, it can be inferred that the transient effect of heat exchange could be very important because the free convective flow is the result of the temperature difference (buoyancy forces). The membrane also affects the flow due to its interaction with the fluid. In a cavity with a membrane, imposing a transient thermal boundary condition to the cavity walls produces a transient flow and heat exchange together with a transient shape of the membrane. For low frequencies of temperature fluctuations, the variation in the shape of the membrane may follow the induced thermal patterns [29]. However, for moderate frequencies of the temperature fluctuations, the response time of the membrane could not be fast as the induced changes in the flow and heat patterns, and hence, the membrane could also act as a filter medium for temperature and flow fluctuations in the cavity.

This paper is a sequel of the author's work [32] on a cavity subdivided by a flexible membrane. The main novelty of the current paper is that we imposed two intrinsic matters; the first is that the cavity is heated by a cyclic thermal boundary condition and the second is the effect of wide range of Prandtl number. It is thought that the results of this paper are fundamental to reveal the incorporation of the transient aspect and the effect of thermal diffusion in the FSI field, which is of interest to many potential applications of flexible walls in the solar collectors industry and fuel cell field.

2. Mathematical modeling

A view of the geometry of the considered problem is shown schematically in Fig. 1 along with the coordinate system and imposed boundary conditions. The dimensions of the enclosure in x^*, y^* coordinates are so much higher than that in z^* one. Accordingly, a two-dimensional scope of the geometry can correctly model the problem. The heat source associated to the hot bound imposes a time-periodic temperature so that $T^* = T^*_c + (T^*_h - T^*_c)$ $(A + B \sin(\omega t))$ while the opposite cold one has the uniform temperature of T^*_c. The lower and upper bounds of the enclosure are thermally impervious. A thin flexible divider is

utilized to partition the enclosure into two smaller ones. The thickness of the divider is t^*_p. The fluid filling the enclosures behaves as an incompressible and Newtonian one. The boundary condition of time-periodic temperature on the left bound necessitates that the flow is unsteady. The present buoyancy-driven flow applies the Boussinesq approximation. This approximation neglects the variations of density except where they are in terms containing the gravity acceleration. Since the flexible divider is thin and with low thermal resistance, the gradient of temperature in it is zero.

Two eyelets of L/100 height are located on the top of the vertical bounds, while the others bounds and the flexible divider are impervious against the mass flow. The goal of the eyelets is to control the fluid flow. The eyelets are considered very small, and hence, the only effect of these eyelets is to balance the pressure in the two sides of the cavity. The densities of the fluid and the flexible divider are the same. The flexible divider behaves as a hyper-elastic material reacting nonlinearly against the imposed forces by the fluid.

2.1 Fluid-Structure Interaction (FSI) model

Description of the reciprocal effects of the fluid and deformable solid material is performed by the known technique of the Arbitrary Lagrangian-Eulerian (ALE). The fluid flow within the enclosure is portrayed by the incompressible mass conservation and the linear momentums equations for the pressure and velocity fields:

$$\nabla^* \cdot \boldsymbol{u}^* = 0 \tag{1}$$

$$\frac{\partial \boldsymbol{u}^*}{\partial t} + \left(\boldsymbol{u}^* - \boldsymbol{w}^*\right) \cdot \nabla^* \boldsymbol{u}^* = -\frac{1}{\rho_f} \nabla^* P^* + \nu_f \nabla^{*2} \boldsymbol{u}^* + \beta \boldsymbol{g} \left(T^* - T_c^*\right) \tag{2}$$

Also, the energy equation which describes the temperature field can be represented as follows:

$$\frac{\partial T^*}{\partial t} + \left(\boldsymbol{u}^* - \boldsymbol{w}^*\right).\nabla^* T^* = \alpha_f \nabla^{*2} T^* \tag{3}$$

The structural deformations of the flexible divider can be achieved by the following nonlinear geometric and elastic formulation:

$$\rho_s \frac{d^2 \boldsymbol{d}_s^*}{dt^2} - \nabla^* \boldsymbol{\sigma}^* = \boldsymbol{F}_v^* \tag{4}$$

$\boldsymbol{F}_v^*$ of the above-written equation is the applied volume forces on the deformable divider, $\boldsymbol{\sigma}^*$ is the solid stress tensor, $\boldsymbol{d}_s^*$ the displacement vector of moving coordinate system so that $d\boldsymbol{d}_s^*/dt = \boldsymbol{w}^*$ and ρ_s is the density of the divider.

In this study, the Neo-Hookean solid model has been utilized for assigning the stress tensor σ^* [33]. This model is applied to characterize the stress-strain nonlinear behavior of a hyper-elastic material with large deformations [33]. The hyper-elastic theory is used more for modeling of rubbery behavior of a polymeric material and polymeric foams that can have large deformations. The model can be written as follows:

$$\boldsymbol{\sigma}^* = J^{-1} F S F^T \tag{5a}$$

where

$$F = \left(I + \nabla^* \boldsymbol{d}_s^*\right), \qquad J = \det(F) \text{ and} \qquad S = \partial W_s / \partial \varepsilon \tag{5b}$$

are the deformation gradient, determinant of the matrix F and the partial differential of the density function of strain energy, respectively. Also, the density function of the strain energy W_s and strain ε is defined through the equations below:

$$W_s = \frac{1}{2}\mu_l \left(J^{-1} I_1 - 3\right) - \mu_l \ln\left(J\right) + \frac{1}{2}\lambda \left(\ln\left(J\right)\right)^2 \tag{6}$$

$$\varepsilon = \frac{1}{2}\left(\nabla^* \boldsymbol{d}_s^{\,*} + \nabla^* \boldsymbol{d}_s^{\,*T} + \nabla^* \boldsymbol{d}_s^{\,*T} \nabla^* \boldsymbol{d}_s^{\,*}\right) \tag{7}$$

λ and μ_l of the above equations, known as Lame's first and second constants, respectively, is related to passion coefficient and elasticity module using 礒= /2(1+ν), and $\lambda = E\nu/(1+\nu)(1-2\nu)$. I_1 is called the first constant of the deformation tensor.

2.2 Boundary conditions

All the bounds of the enclosure are motionless ($u^* = v^* = 0$). The lower and topper bounds of the both sub-cavities are thermally insulated ($\partial T^*/\partial y^* = 0$). The right hand wall is at the constant temperature $T^* = T^*_c$, while a time-sinusoidal function of temperature is imposed on the left hand wall such that the period-averaged of it is $A(T^*_h - T^*_c) + T^*_c$. This function is written in the term of $T^* = T^*_c + (T^*_h - T^*_c)(A + B\sin(\omega t))$ where ω shows the oscillation frequency and values of A and B are 1 and 0.1, respectively.

Along the fluid-solid interface, continuity of the dynamic motion and kinematic forces are the boundary conditions utilized to model the fluid and deformable divider interaction. These conditions can be represented as

$$\frac{\partial \boldsymbol{d}_s^{\,*}}{\partial t} = \boldsymbol{u}^* \text{ and } \boldsymbol{\sigma}^*.n = -P^* + \mu_f \nabla^* \boldsymbol{u}^* \tag{8}$$

Applying the conservation of energy on the flexible divider along with the previously assumptions results in the equation below:

$$\frac{\partial T^{*+}}{\partial n} = \frac{\partial T^{*-}}{\partial n} \tag{9}$$

In this equation, the plus and minus marks denote the right and left sides of the deformable divider, respectively. Also, the boundary condition for both eyelets can be represented as follows:

$$\left[-P^* + \mu_f \nabla^* \boldsymbol{u}^*\right].n = 0 \tag{10}$$

2.3 Dimensionalizing the governing equations and boundary conditions

To provide with dimensions, non-dimensional parameters are introduced below;

$$\boldsymbol{d}_s = \frac{\boldsymbol{d}_s^*}{L}, \qquad \boldsymbol{\sigma} = \frac{\boldsymbol{\sigma}^*}{E}, \qquad \tau = \frac{t\alpha_f}{L^2}, \qquad (x, y) = \frac{\left(x^*, y^*\right)}{L}, \tag{11a}$$

$$\boldsymbol{u} = \frac{\boldsymbol{u}^* L}{\alpha_f}, \qquad \boldsymbol{w} = \frac{\boldsymbol{w}^* L}{\alpha_f}, \qquad P = \frac{L^2}{\rho_f \alpha_f^2} P^*, \quad T = \frac{T^* - T_c^*}{T_h^* - T_c^*} \tag{11b}$$

$$\nabla = \frac{\nabla^*}{1/L}, \qquad \nabla^2 = \frac{\nabla^{*2}}{1/L^2}, \qquad t_p = \frac{t_p^*}{L} \tag{11c}$$

To dimensionalize the equations, the above parameters are substituted for the Eqs. (1)-(4). Therefore, we then have,

$$\frac{1}{\rho_R} \frac{d^2 \boldsymbol{d}_s}{d\tau^2} - E_\tau \nabla \boldsymbol{\sigma} = E_\tau \boldsymbol{F}_v \tag{12}$$

$$\nabla \boldsymbol{u} = 0 \tag{13}$$

$$\frac{\partial \boldsymbol{u}}{\partial \tau} + \left(\boldsymbol{u} - \boldsymbol{w}\right) \cdot \nabla \boldsymbol{u} = -\nabla P + Pr \nabla^2 \boldsymbol{u} + Pr \boldsymbol{Ra} T \tag{14}$$

$$\frac{\partial T}{\partial \tau} + \left(\boldsymbol{u} - \boldsymbol{w}\right).\nabla T = \nabla^2 T \tag{15}$$

where

$$\boldsymbol{Ra} = \frac{\mathbf{g}\beta\left(T_h^* - T_c^*\right)L^3}{\upsilon_f \alpha_f}, Pr = \frac{\upsilon_f}{\alpha_f}, E_\tau = \frac{EL^2}{\rho_f \alpha_f^2}, \boldsymbol{F}_v = \frac{\left(\rho_f - \rho_s\right)L\mathbf{g}}{E}, \rho_R = \frac{\rho_f}{\rho_s} \tag{16}$$

The vectors of $\boldsymbol{Ra}$ and $\boldsymbol{F_v}$ act in the direction of the *y*-axis, upwards and downwards, respectively. Since the Rayleigh number includes the vector of gravitation acceleration, it has been represented as a vector. Indeed, the Rayleigh numbers in the *x* and y directions are, respectively, zero and $Ra = |\boldsymbol{Ra}|$.

Finally, the non-dimensional forms of the velocities and temperatures on the bounds are

x=0 $\quad u = v = 0$ and $T = A + B\sin(f\,\tau)$ (17a)

x=1 $\quad u = v = 0$ and $T = 0$ (17b)

y=0 $\quad u = v = 0$ and $\partial T/\partial y = 0 = 0$ (17c)

y=1 $\quad u = v = 0$ and $\partial T/\partial y = 0 = 0$ (17d)

For the membrane $\partial T^{+}/\partial n = \partial T^{-}/\partial n$ and $T^{+} = T^{-}$ (17e)

For the fluid-solid interface $\partial \boldsymbol{d}_s/\partial\tau = \mathbf{u}$ and $E_\tau \boldsymbol{\sigma}.n = -P + Pr\nabla\boldsymbol{u}$ (17f)

For both of the eyelets $\left[-P + Pr\nabla\boldsymbol{u}\right].n = 0$ (17g)

where the dimensionless frequency of the periodic temperature is defined as $f = \omega L^2/\alpha_f$

Here, two definitions are expressed in order to evaluate the rate if heat transfer rate: first, the average Nusselt number along the left or the right side walls at a specified time is

$$Nu_{av} = -\int_0^1 \frac{\partial T}{\partial x} dy \tag{18}$$

Secondary, the average Nusselt number in one period of time is defined as

$$Nu_{av\,T_p} = -\int_{nT_p}^{(n+1)T_p} \int_0^1 \frac{\partial T}{\partial x} dy d\tau \tag{19}$$

where n and T_p are the number of periods and the period, respectively. Also, the dimensionless mean temperature in the whole enclosure is calculated as follows:

$$T_{av} = \frac{\int_A T_{local} dA}{\int_A dA} \tag{20}$$

Here, A denotes the domain of the enclosure. To describe the fluid flow inside the sub-cavities the concept of the stream function can be used as FOLLOWS:

$$u = \frac{\partial \psi}{\partial y}, \quad v = -\frac{\partial \psi}{\partial x} \tag{21}$$

3. Numerical approach, grid independence test and validation

The interdependent, complex and non-linear Eqs. (12)-(15) are solved by employing the Galerkin finite element approach with the aid of ALE technique. The numerical approach of finite element are expressed in [34, 35] in details. A mesh of non-uniform triangular elements is employed to discretize the domain.

For as much as the results of the numerical solutions depend on the number of grid cells, firstly; it must be proven that the results are independent of the grid size. In the present investigation, a grid independence test has been done. A grid independence study has been done for the mean Nusselt number in a period of oscillation and the dimensionless temperature at point A with the position of $x = 0.025$ and y = 0 next to the flexible bound when $Ra = 10^7$, $E_\tau = 10^{13}$, $Pr = 6.2$ and $f = 20\pi$. The increase of the Rayleigh number enhances the strength of the convection regime and reduces the thickness of the boundary layer which, as a result, boosts the gradients of the temperature and velocity in the vicinity of the enclosure walls. The increase of the stiffness of the membrane also increases the tension gradients in the membrane. The Prandtl number of 6.2 is common in the literature, and it is close to the Prandtl number of water. The set of $Ra = 10^7$, $E_\tau = 10^{13}$ indicates the most sensitive case in the present study. Thus, the grid check has been performed for this set of non-dimensional variables.

Fig. 2 shows the general and zoom views of the selected grid. Fig. 3 shows the temperature at the coordinate of A ($x = 0.025$, $y = 0$) for several meshes of different sizes.

The results presented in Table 1 as well as the temperature time series of point A defined in Fig. 3 clearly shows that the grid of size 11406 elements is appropriate to be used for the process of numerical simulation.

For more confirmation of the accuracy of the current modeling and simulation, the used solution method has been employed to resolve several problems investigated by previous researchers. In the first validation, the results obtained in this study and the those by Xu *et al*. [21] have been compared. Xu *et al*. [21] have studied the heat transfer of a transient free convection in an enclosure divided into two parts using a rigid partition. It is worth mentioning that in the work of Xu *et al*. [21], the variables Ra, Pr and τ are defined as $\boldsymbol{Ra} = \mathbf{g}\beta\left(T_h^* - T_c^*\right)L^3 \big/ \upsilon_f \alpha_f$, $Pr = \upsilon_f / \alpha_f$ and $\tau = t\alpha_f Ra^2 \big/ L^2$, respectively. As can be seen from Fig. 4, there is an excellent agreement between the outcomes of this work and those reported in [21]. This validation verifies the sufficiency of the present formulation and solution to simulate the transient natural convection in the fluid domain and the partition.

Another validation is the comparison of the deformation of the lower bound of a lid-driven enclosure computed by the present study and that computed by Küttler and Wall [23]. The schematic view of the study of Küttler and Wall [23] along with the utilized physical values have been depicted inside Fig. 5. In the work of them [23], the bottom bound was flexible and the induced flow due to the lid movements would change the configuration of the bound. From Fig. 5, it can be observed that the current solution method is highly acceptable. This comparison confirms the capability of the present formulation and the solution for dealing with the FSI physics in an ALE system of meshing.

The last validation compares the experimental outcomes reported by Tatsuo *et al*. [17] and the numerical results calculated of this investigation. Also, the validation compares our results and Churchill's relation [36]. As previously mentioned, Tatsuo *et al*. [17] did an experimental research on free convection in a regular quadrilateral divided vertically by N multiplex rigid plates. In the case of N=1 and Ar=4 (height/length), the study of Tatsuo *et al*. [17] is very similar to the present study. From Fig. 6, obviously, it is established a great accordance between the experimental outcomes and Churchill's relation. This comparison confirms the correctness of the results from the natural convection heat transfer point of view for the large values of τ where the convective heat transfer reaches to its steady-state form.

4. Results and discussion

Here, the impacts of the dimensionless parameters of Rayleigh number ($10^4 \leq Ra \leq 10^7$), elasticity modulus ($5\times10^{12} \leq E_\tau \leq 10^{16}$) and the frequency ($2\pi \leq f \leq 40\pi$) on the rate of heat transfer, stress in the solid flexible partition and the patterns of the flow and temperature domains are investigated. The values considered for Pr are 0.71, 6.2 and 200. In fact, these values correspond to the working fluids of air, water and engine oil, respectively. As discussed by Markatos and Pericleous [7], for a regular square cavity, the critical Rayleigh number starts from 10^6, and for a Rayleigh number higher than this value, the transient phenomenon can be expected. However, it should be noticed that the presence of the membrane, acting as a partition, suspends the commencing of the transient phenomenon to much higher Rayleigh numbers. For instance, Xu et al. [21] addressed the heat transfer of laminar free convection in a square enclosure partitioned into two equal parts by a rigid partition for a Rayleigh number up to 9.2×10^8.

4.1 Effects of Rayleigh number

In the current category, the dimensionless parameters $E_{\tau,}$ $f,$ and Pr are fixed at $10^{13,}$ 10π, and 6.2, respectively while the Rayleigh number Ra varies from 10^4 to 10^7. Figure 5 shows the streamlines for the mentioned range of Ra in different periods of oscillation. As envisaged, the maximum value of stream function $|\psi|_{max,}$ introduced as the intensity of the flow, increases as Ra increases. In fact, this result is referred to the fact that an increase of Ra enhances the buoyancy force in the momentum equation. This effect can be seen in the four considered periods of oscillation. In addition, a single clockwise (CW) circulation (negative stream function) is formed in the cases of low Ra values (Ra =10^4 and 10^5) in both sub-cavities. However, at high Ra numbers (Ra =10^6 and 10^7), the CW vortex created in the right part of enclosure becomes stronger and as a result, it breaks up into two vortices. Hence, the fluid-solid interaction forces increase slowly e until deforming the impermeable flexible membrane to the left as shown in Fig. 7. It is worth mentioning that the streamlines get crowded close to the flexible membrane, which indicates an intensified flow there. Besides, at lower $Ra,$ the intensity of the flowing fluid is relatively weak and the pressure is approximately identical in both sub-cavities, and therefore, the deformation of the flexible membrane is marginal.

The corresponding isotherms contours are presented in Fig. 8. These contours demonstrate the variation of the heat transfer mechanism as Ra is varying. The isotherms tend to possess a stratification pattern as Ra increases. This outcome is attributed to the augmentation of the strengthening of the convective currents as result of the augmentation of the buoyancy forces. Additionally, Fig. 8 states that at Ra = 10^4 the isotherms look mostly vertical, which is an indication to the dominance of the conduction mode against the convection one. As Ra increases, the impact of the conduction mechanism diminishes while the effect of the convection mode increases. In general, the onset of the buoyancy force dominance can be characterized when the isotherms are mostly horizontal and the membrane is deformed noticeably, this can be seen at Ra = 10^6.

Figures 9 (a)-(b) and 10 present, respectively, the evolution of the average Nusselt number Nu_{av}, average temperature T_{av}, and the maximum stress σ_{max} in the flexible membrane for Pr = 6.2, f = 10π and E_τ =10^{13}. They are monitored after one cycle of the

temperature oscillation ($\tau = 0.2$). From Fig. 9 (a) and (b), Nu_{av} (as a representation of the convective heat flux) and T_{av} vary in a sinusoidal fashion. The average Nusselt number doubles for each one order of magnitude of the Rayleigh number. In addition, these figures show that an increase of Ra leads to an enhancement of the oscillation range of both Nu_{av} and T_{av} functions. Also, it is clear that with increasing Ra, the increased heat transfer rate (Nu_{av}) reduces T_{av}. Figure 10 illustrates that σ_{max} extremely enhances with an increase of Ra. In the case of $Ra = 10^4$, σ_{max} is almost constant. In this case, the maximum stress in the flexible membrane is in order of 10^{10}, while it is clear that the oscillation function of σ_{max} is amplified as Ra increased. This can be attributed to the increasing deflection of the flexible membrane with Ra.

4.2 Effects of Prandtl number (Pr)

The effects of Pr on the streamlines and isotherms contours in five periods of oscillation are displayed in Figs. 11 and 12, respectively, for $Ra = 10^7$, $E_\tau = 10^{14}$, and $f = 10\pi$. Increasing the Prandtl number means increasing the momentum diffusion over the heat diffusion, and as a result, it is clear from Fig. 11, that in all periods of oscillation, the intensity of the flowing fluid increases with increasing values of Pr which in turn, significantly stretches the flexible membrane to the right. Also, it can be seen that the stretching of the flexible membrane grows slightly as time increases.

Figure 12 (whose parameters are the same as those labeled in Fig. 11) shows that the isotherms follow the variations of the streamlines completely for all Prandtl numbers and times. In other words, the volumes of the warm (left) and cold (right) regions shrink and expand, respectively as Pr increases.

The variations of Nu_{av} and T_{av} inside the whole cavity are shown in Figs. 13 (a) and (b). For better presentation of the results, the variations of Nu_{av} and T_{av} have been depicted in several periods of oscillation. As portrayed in Fig. 13 (a), the increase of Pr enhances the momentum exchange between the fluid molecules which in turn enhances the average Nusselt number Nu_{av}. In comparison with $Pr = 0.71$ (air), the amplitude of graphs with $Pr = 6.2$ (water) and $Pr = 200$ (engine oil) enhances 8.2 % and 22.5 %, respectively. According to these observations of Nu_{av}, Fig. 13 (b) shows clearly that the T_{av} inside the whole

enclosure decreases as Pr increases. Here, unlike the trend of the Nu_{av}, the sinusoidal graphs of the average temperature shift downwards and also, their amplitudes decrease with increasing values of Pr. This reduction of the amplitude based on the amplitude of the sinusoidal function results for Pr = 0.71 equals to 1.15 (with water) and 23.3 % (with engine oil).

The variations of the maximum stress σ_{max} in the flexible membrane versus the dimensionless time for several values of the Prandtl number are represented in Fig. 14. The results state that the value of σ_{max} increases extremely when the Pr grows. The reason for this is that strengthening of the fluid recirculation within the two sub-cavities. It is interesting to know that the enhancement of the amplitude of the sinusoidal variations of σ_{max} is 447.8 % and 15453 % for water and engine oil, respectively compared with air.

4.3 Effects of temperature oscillation frequency

Figures 15 and 16 illustrates the efficacies of the oscillating temperature frequency on the flow and temperature fields, respectively while the other parameters are fixed at Ra =10^7, E_τ = 10^{14} and Pr = 6.2. As can be observed from the streamlines patterns, the frequency influences the strength of the fluid flow while the patterns of the streamlines are indiscernible. Also, there are no noticeable variations in the streamlines trend with the different times. At a specific time, the frequency increases the strength of flow ($\tau = T_p$) while at another time, there is no certain trend (for example $\tau = T_p+3T_p/4$). According to the corresponding isotherms (Fig. 16), we conclude that in the left sub-cavity, the isotherms move up with the frequency when $\tau =T_p$ and $T_p+T_p/4$; while if τ is $nT_p+T_p/2$ or $nT_p+3T_p/4$, the isotherms shift downward as the frequency augments.

From Figs. 17 (a) and (b), obviously, the frequency increment decreases both the amplitude of the Nu_{av} and T_{av} for Ra = 10^7, Pr = 6.2 and E_τ = 10^{14}. The Nusselt number and the average temperature time functions for all frequency values oscillate around certain values which are 8.1 and 0.435, respectively. Therefore, it can be concluded that the frequency influences only the amplitude of the Nu_{av} and T_{av} as time functions and has no effect on the period-averaged Nu_{av} and T_{av}. The graph of the maximum stress in the flexible membrane shown in Fig. 18 also follows the trend of Nu_{av} and T_{av} with the frequency.

Accordingly, it seems that when f tends to infinity, the amplitude of the oscillatory functions mentioned approaches constant values. Physically, when f tends to infinity, the left wall temperature oscillates very quickly so that the fluid does not have enough time to receive the temperature oscillation effects.

4.4 Effects of elasticity modulus

The thermal and dynamical behaviors of the fluid under the influence of the variation of the elasticity modulus are presented in Figs. 19 and 20. In these figures, each of the vertical columns illustrates the flow and temperature fields at a specific time. For all elasticity modulus values, the intensified fluid flow occurs in the second column, at a period of oscillation equals to $nT_p+T_p/4$. For a low value of the elasticity modulus, the flexible wall experiences substantial deformation when faster circulated fluid exerts larger forces, as such, the highest flexible membrane stretching is noticed for the lower values of the elasticity modulus. The stretched membrane results in a substantial space available for the right sub-cavity, thus, the highest fluid flow intensity is recorded for the lower elasticity modulus. The vortex created in the left part of the enclosure for the lowest elasticity modulus ($E_\tau = 5\times10^{12}$) case breaks into two vortices when E_τ changes from $E_\tau = 5\times10^{12}$ to $E_\tau = 10^{13}$. After that, the general patterns of the streamlines are the same for all values of the elasticity modulus. Figure 20 shows that the isotherms contours are formed in accordance with the streamline patterns. Among the times defined for displaying the streamlines and the isotherms, the maximum temperature is observed at $nT_p+T_p/4$.

Figures 21 (a) and (b) display the variations of Nu_{av} and T_{av} versus several periods of oscillation for different values of E_τ. In general, it can be stated that the Nu_{av} decreases and T_{av} augments with the increase of the elasticity modulus. But it should be noted that the reduction and augmentation rate of Nu_{av} and T_{av} decay when the value of E_τ is higher than $E_\tau = 10^{14}$. In order to justify these behaviors, it can be said that when the elasticity modulus of the membrane is low, an interaction between the solid material and the fluid takes place, the movement of the membrane is easier and more in a period of oscillation; hence, some fluid exit from the embedded eyelets. This quantity of fluid is substituted by some cold and fresh fluid. But when the elasticity modulus is high, the deflection of the

flexible partition is restricted; consequently, the fluid entry and exit cannot be seen significantly. This claim is proven by the representation of the discharge or charge of the enclosure through the eyelets in Fig. 22. In Fig. 22, Q is the dimensionless flow rate through the left eyelet. The negative and positive values of Q depict the intake and the discharge of the fluid through the eyelets.

Finally, Fig. 23 provides information about the variations of σ_{max} versus the oscillation period for different values of E_τ when $Ra = 10^7$, $f = 10\pi$ and $Pr = 6.2$. The obtained results show a noticeable increase of the maximum stress in the membrane σ_{max} with the increase of E_τ. This is because the increase of the elasticity modulus gives rise to the stiffness of the membrane wall, which in turn leads to much high resistance against the force exerted by the fluid circulation. In addition, the oscillation amplitude of σ_{max} increases as E_τ is increased.

5. Conclusions

The investigated problem in this work is a fluid-structure interaction (FSI) representing a periodically-heated square cavity equally divided vertically by a flexible membrane. The left vertical wall is exposed to a sinusoidal time-varying temperature, while the right surface is kept isothermal at a cold temperature. There is no thermal diffusion from the upper and lower horizontal boundaries. The interdependent, complex and non-linear governing equations are solved by employing the Galerkin finite element approach with the aid of ALE technique. Four pertinent parameters are altered in this study. According to these studied parameters, the following concluding remarks are drawn:

1- Due to the applied boundary conditions, the general behavior of the flexible partition is stretched to the left, resulting in shrinking the left sub-cavity and expanding the right one.

2- A fluid with a high Prandtl number enhances the convective heat transfer, robustly stretches the flexible membrane, and as a result, increases the associated maximum stress.

3- The lower elasticity modulus of the flexible membrane is, the higher are the flexible partition deflection, mean Nusselt number and the maximum stress of the partition.

4- The frequency of the oscillating left wall temperature does not affect the deformation and the stress of the flexible membrane, the Nu_{av} and T_{av}. Nevertheless, the amplitudes of Nu_{av}, T_{av}, and σ_{max} are decreasing functions of the wall temperature frequency.

5- The periodic state values of both the Nu_{av} and σ_{max} of the flexible partition increase significantly with the increase of Ra.

Acknowledgements

The third author is grateful to Dezful Branch, Islamic Azad University, Dezful, Iran for its financial support. The first author acknowledges the Young Researchers and Elite Club, Yasooj Branch, Islamic Azad University, Yasooj, Iran for its financial support.

References

[1] A. Emery, "Free Convection Through Vertical Plane Layers—Moderate and High Pranitl limber Fluids," 1969.

[2] G. de Vahl Davis, "Natural convection of air in a square cavity: a bench mark numerical solution," *International Journal for numerical methods in fluids,* vol. 3, pp. 249-264, 1983.

[3] J. C. Patterson and S. Armfield, "Transient features of natural convection in a cavity," *Journal of Fluid Mechanics,* vol. 219, pp. 469-497, 1990.

[4] K. M. Kelkar and S. V. Patankar, "Numerical prediction of natural convection in square partitioned enclosures," *Numerical heat transfer,* vol. 17, pp. 269-285, 1990.

[5] M. Ciofalo and T. Karayiannis, "Natural convection heat transfer in a partially—or completely—partitioned vertical rectangular enclosure," *International journal of Heat and Mass transfer,* vol. 34, pp. 167-179, 1991.

[6] T. Fusegi, J. Hyun, K. Kuwahara, and B. Farouk, "A numerical study of three-dimensional natural convection in a differentially heated cubical enclosure," *International Journal of Heat and Mass Transfer,* vol. 34, pp. 1543-1557, 1991.

[7] N. C. Markatos and K. Pericleous, "Laminar and turbulent natural convection in an enclosed cavity," *International Journal of Heat and Mass Transfer,* vol. 27, pp. 755-772, 1984.

[8] R. Kuyper, T. H. Van Der Meer, C. Hoogendoorn, and R. Henkes, "Numerical study of laminar and turbulent natural convection in an inclined square cavity," *International Journal of Heat and Mass Transfer,* vol. 36, pp. 2899-2911, 1993.

[9] G. Barakos, E. Mitsoulis, and D. Assimacopoulos, "Natural convection flow in a square cavity revisited: laminar and turbulent models with wall functions," *International Journal for Numerical Methods in Fluids,* vol. 18, pp. 695-719, 1994.

[10] A. Baïri, E. Zarco-Pernia, and J.-M. G. De María, "A review on natural convection in enclosures for engineering applications. The particular case of the parallelogrammic diode cavity," *Applied Thermal Engineering,* vol. 63, pp. 304-322, 2014.

[11] A. Ben-Nakhi and A. J. Chamkha, "Effect of length and inclination of a thin fin on natural convection in a square enclosure," *Numerical Heat Transfer,* vol. 50, pp. 381-399, 2006.
[12] A. Ben-Nakhi and A. J. Chamkha, "Conjugate natural convection in a square enclosure with inclined thin fin of arbitrary length," *International journal of thermal sciences,* vol. 46, pp. 467-478, 2007.
[13] A. J. Chamkha and M. A. Ismael, "Natural convection in differentially heated partially porous layered cavities filled with a nanofluid," *Numerical Heat Transfer, Part A: Applications,* vol. 65, pp. 1089-1113, 2014.
[14] M. Sheikholeslami, M. Rashidi, T. Hayat, and D. Ganji, "Free convection of magnetic nanofluid considering MFD viscosity effect," *Journal of Molecular Liquids,* vol. 218, pp. 393-399, 2016.
[15] M. Mansour, A. Chamkha, and M. Bakier, "Magnetohydrodynamic Natural Convection and Entropy Generation of a Cu-Water Nanofluid in a Cavity with Wall Mounted Heat Source/Sink," *Journal of Nanofluids,* vol. 4, pp. 254-269, 2015.
[16] Y. Varol, H. F. Oztop, and I. Pop, "Natural convection in a diagonally divided square cavity filled with a porous medium," *International Journal of Thermal Sciences,* vol. 48, pp. 1405-1415, 2009.
[17] N. Tatsuo, S. Mitsuhiro, and K. Yuji, "Natural convection heat transfer in enclosures with an off-center partition," *International journal of heat and mass transfer,* vol. 30, pp. 1756-1758, 1987.
[18] T. Nishimura, M. Shiraishi, F. Nagasawa, and Y. Kawamura, "Natural convection heat transfer in enclosures with multiple vertical partitions," *International Journal of Heat and Mass Transfer,* vol. 31, pp. 1679-1686, 1988.
[19] H. F. Oztop, Y. Varol, and A. Koca, "Natural convection in a vertically divided square enclosure by a solid partition into air and water regions," *International Journal of Heat and Mass Transfer,* vol. 52, pp. 5909-5921, 2009.
[20] K. Kahveci, "Natural convection in a partitioned vertical enclosure heated with a uniform heat flux," *Journal of heat transfer,* vol. 129, pp. 717-726, 2007.
[21] F. Xu, J. C. Patterson, and C. Lei, "Heat transfer through coupled thermal boundary layers induced by a suddenly generated temperature difference," *International Journal of Heat and Mass Transfer,* vol. 52, pp. 4966-4975, 2009.
[22] E. Kalabin, M. Kanashina, and P. Zubkov, "Natural-convective heat transfer in a square cavity with time-varying side-wall temperature," *Numerical Heat Transfer, Part A: Applications,* vol. 47, pp. 621-631, 2005.
[23] U. Küttler and W. A. Wall, "Fixed-point fluid–structure interaction solvers with dynamic relaxation," *Computational Mechanics,* vol. 43, pp. 61-72, 2008.
[24] M. Engel and M. Griebel, "Flow simulation on moving boundary-fitted grids and application to fluid–structure interaction problems," *International journal for numerical methods in fluids,* vol. 50, pp. 437-468, 2006.
[25] R. Van Loon, P. Anderson, F. Van de Vosse, and S. Sherwin, "Comparison of various fluid–structure interaction methods for deformable bodies," *Computers & structures,* vol. 85, pp. 833-843, 2007.
[26] W.-S. Fu and C.-P. Huang, "Effects of a vibrational heat surface on natural convection in a vertical channel flow," *International journal of heat and mass transfer,* vol. 49, pp. 1340-1349, 2006.
[27] J. Lee, J. Shin, and S. Lee, "Fluid–structure interaction of a flapping flexible plate in quiescent fluid," *Computers & Fluids,* vol. 57, pp. 124-137, 2012.
[28] A. Kalmbach and M. Breuer, "Experimental PIV/V3V measurements of vortex-induced fluid–structure interaction in turbulent flow—A new benchmark FSI-PfS-2a," *Journal of Fluids and Structures,* vol. 42, pp. 369-387, 2013.

[29] G. De Nayer and M. Breuer, "Numerical FSI investigation based on LES: Flow past a cylinder with a flexible splitter plate involving large deformations (FSI-PfS-2a)," *International Journal of Heat and Fluid Flow,* vol. 50, pp. 300-315, 2014.
[30] M. Ghalambaz, E. Jamesahar, M. A. Ismael, and A. J. Chamkha, "Fluid-structure interaction study of natural convection heat transfer over a flexible oscillating fin in a square cavity," *International Journal of Thermal Sciences,* vol. 111, pp. 256-273, 2017.
[31] E. Jamesahar, M. Ghalambaz, and A. J. Chamkha, "Fluid–solid interaction in natural convection heat transfer in a square cavity with a perfectly thermal-conductive flexible diagonal partition," *International Journal of Heat and Mass Transfer,* vol. 100, pp. 303-319, 2016.
[32] S. Mehryan, M. Ghalambaz, M. A. Ismael, and A. J. Chamkha, "Analysis of fluid-solid interaction in MHD natural convection in a square cavity equally partitioned by a vertical flexible membrane," *Journal of Magnetism and Magnetic Materials,* vol. 424, pp. 161-173, 2017.
[33] R. W. Ogden, *Non-linear elastic deformations*: Courier Corporation, 1997.
[34] J. Donea and A. Huerta, *Finite element methods for flow problems*: John Wiley & Sons, 2003.
[35] T. Basak and A. J. Chamkha, "Heatline analysis on natural convection for nanofluids confined within square cavities with various thermal boundary conditions," *International Journal of Heat and Mass Transfer,* vol. 55, pp. 5526-5543, 2012.
[36] S. Churchill, "Free convection in layers and enclosures," *Heat exchanger design handbook,* vol. 2, 1983.

Table 1. Grid independency test for $Ra = 10^7$, $E_\tau = 10^{13}$, $f = 20\pi$ and $Pr = 6.2$

cases	The number of elements	Nu_{av,T_p}	The average of error (%) *
1	3064	84.06	
2	5644	82.15	1.91

3	8575	81.45	0.70
4	11406	81.10	0.35
5	16302	80.74	0.36
6	20158	80.75	0.10

* $\text{Error} = \left| Nu_{av,T_p,i+1} - Nu_{av,T_p,i} \right| \Big/ \left| Nu_{av,T_p,i} \right|$

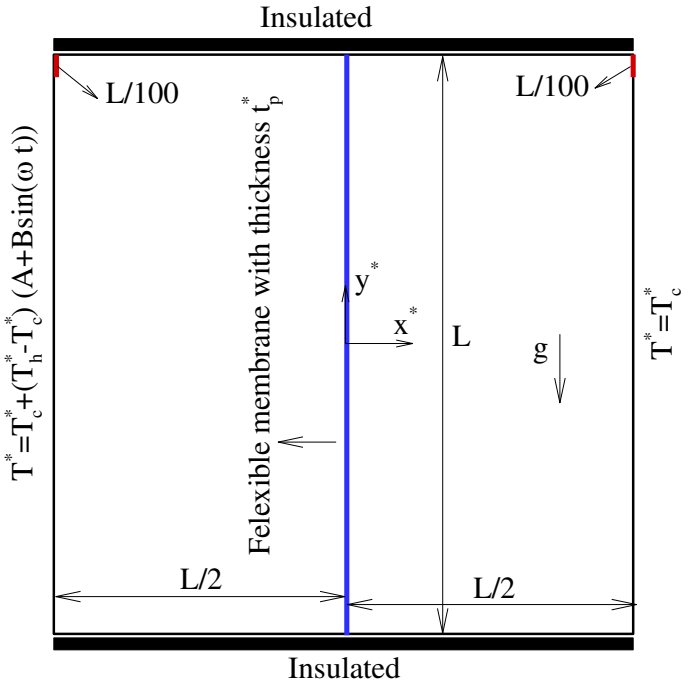

Fig. 1. Physical problem and coordinate system

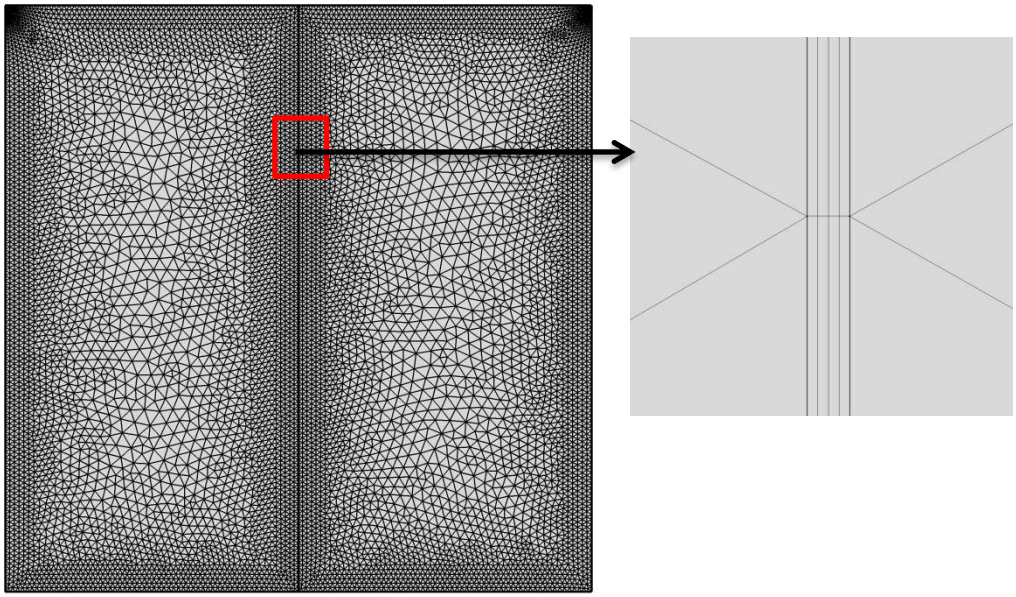

Fig. 2 General and zoom views of the grid selected

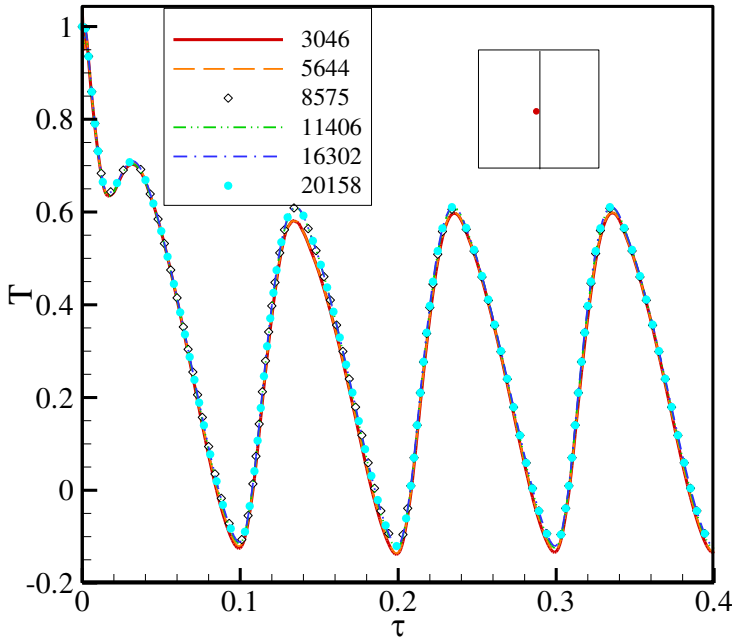

Fig. 3 Time series of the dimensionless temperature at point A ($x = 0.025$, $y = 0$) obtained in different grids

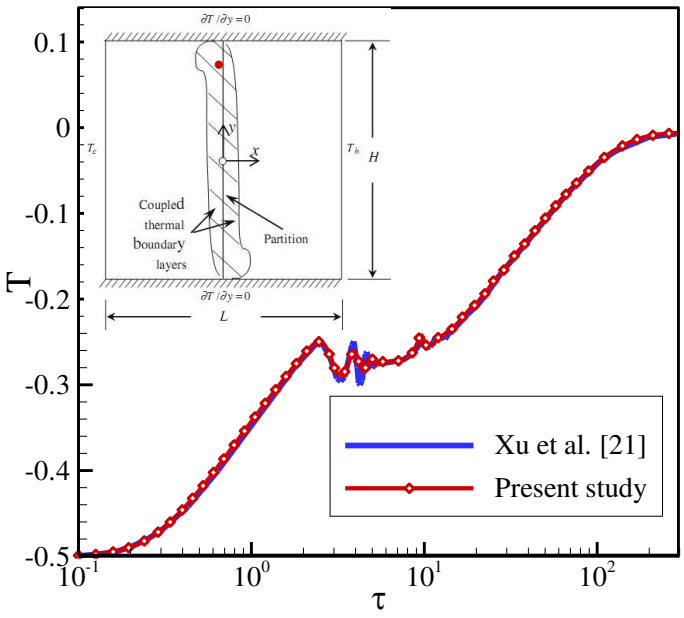

Fig. 4. Comparison of the dimensionless temperature reported by Xu *et al.* [21] and this study at the certain point (0.0083, 0.375)

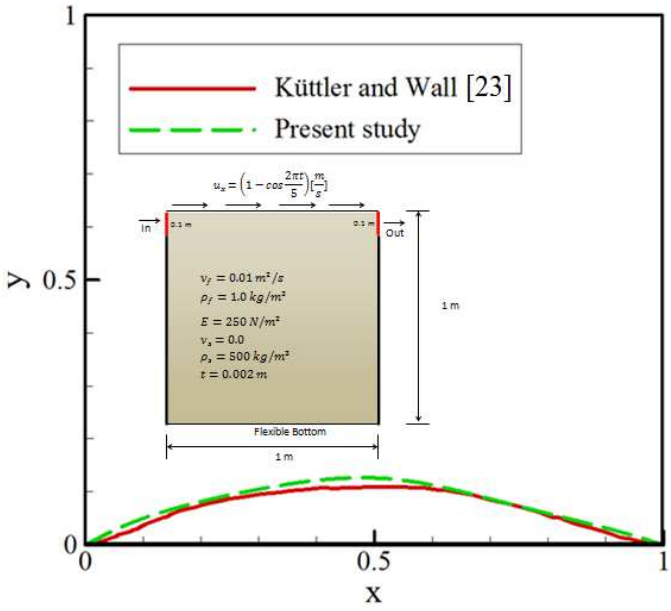

Fig. 5. The deformation of the flexible bottom wall of the lid-driven cavity perused by Küttler and Wall [23] and the present study at t =7.5s

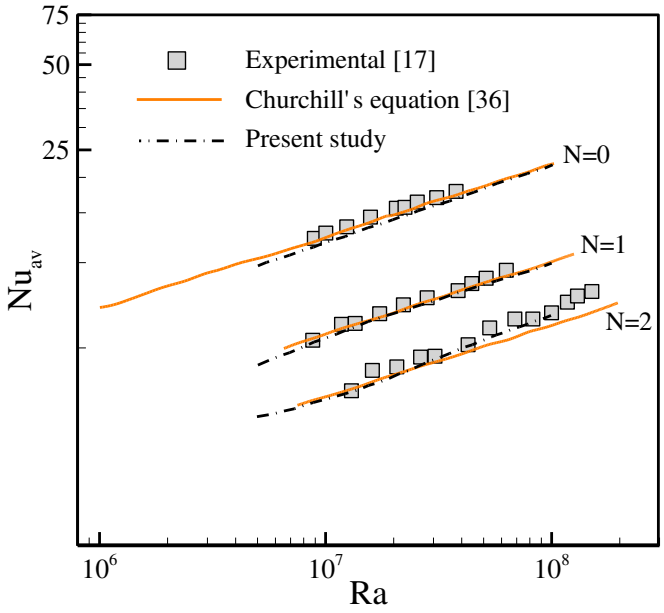

Fig. 6. The comparison of average Nusselt between the results of present study and experimental results reported by Tatsuo et al. [17] and Churchill's relation [36] at $Pr = 6$ and $Ar = 4$

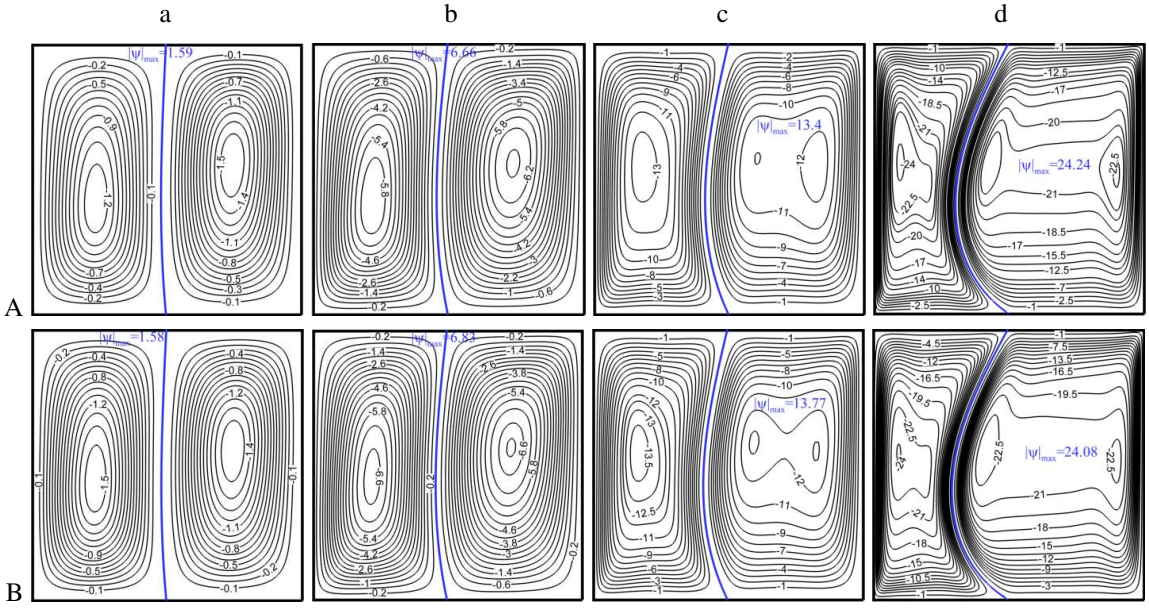

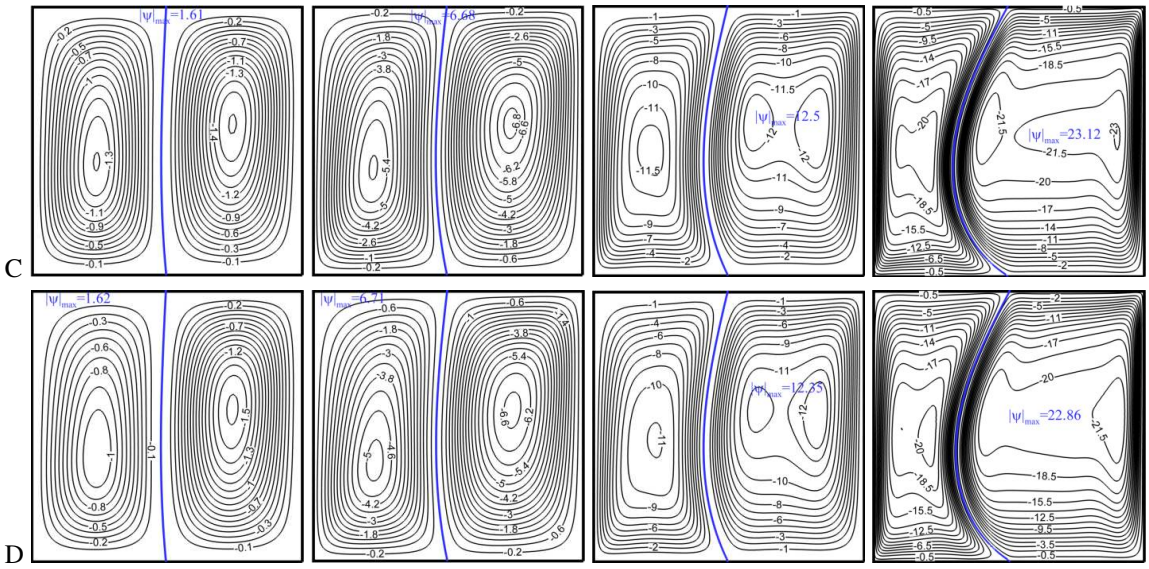

Fig. 7. Streamlines patterns for the cavities with Rayleigh numbers a: $Ra = 10^4$, b: $Ra = 10^5$, c: $Ra = 10^6$, and d: $Ra = 10^7$ in a period of oscillation (A: nT_p, B: $nT_p+T_p/4$, C: $nT_p+T_p/2$, D: $nT_p+3T_p/4$) for $f = 10\pi$, $E_\tau = 10^{13}$ and $Pr = 6.2$

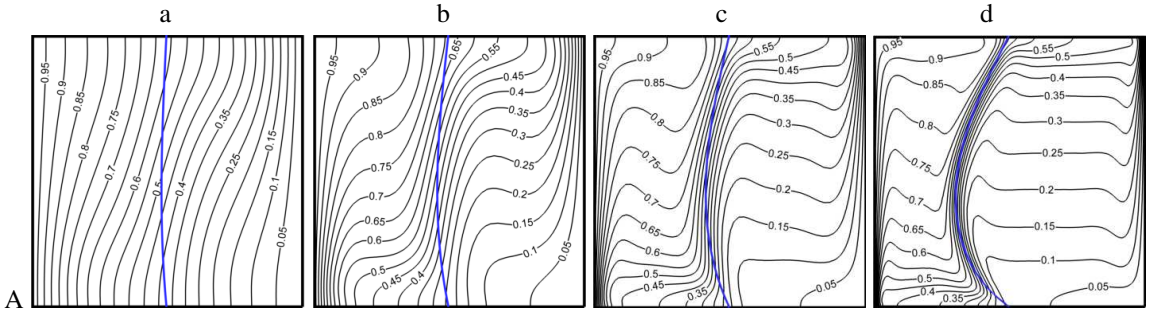

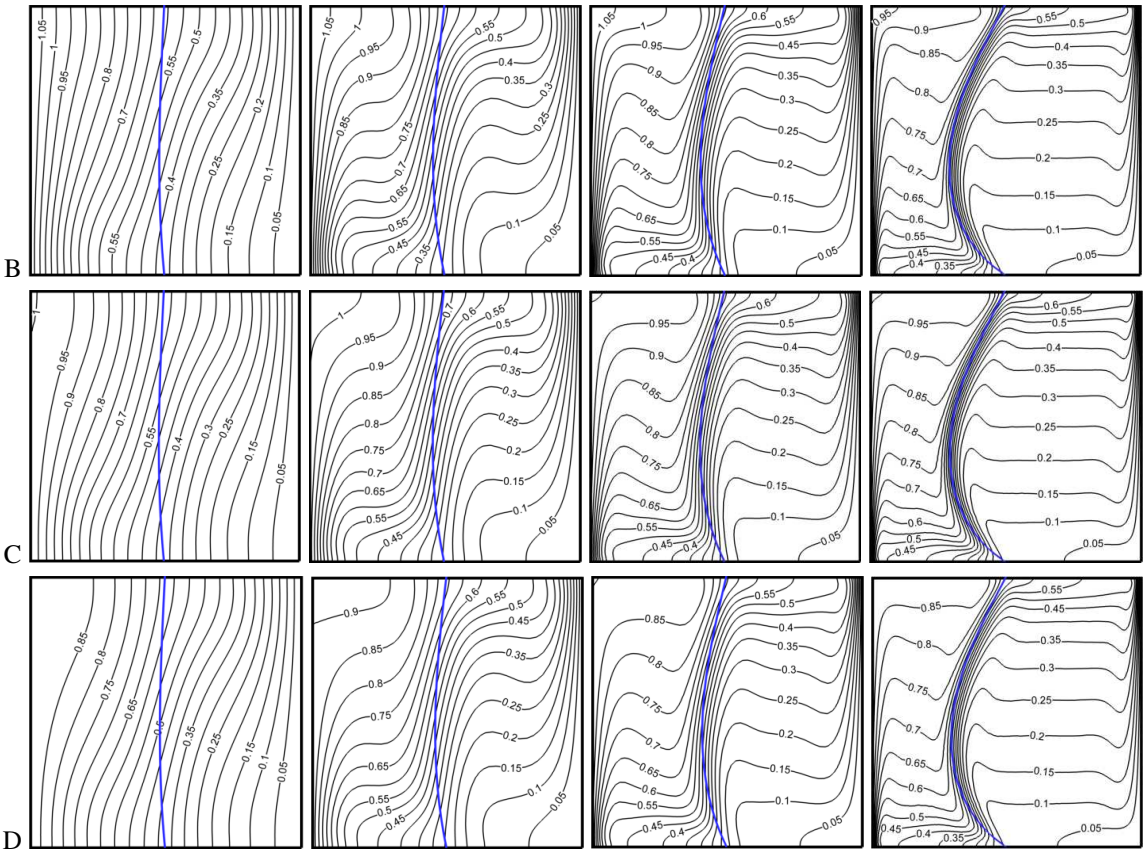

Fig. 8. Isotherms patterns for the cavities with Rayleigh numbers a: $Ra = 10^4$, b: $Ra = 10^5$, c: $Ra = 10^6$, and d: $Ra = 10^7$ in a period of oscillation (A: nT_p, B: $nT_p+T_p/4$, C: $nT_p+T_p/2$, D: $nT_p+3T_p/4$) for $f = 10\pi$, $E_\tau = 10^{13}$ and $Pr = 6.2$

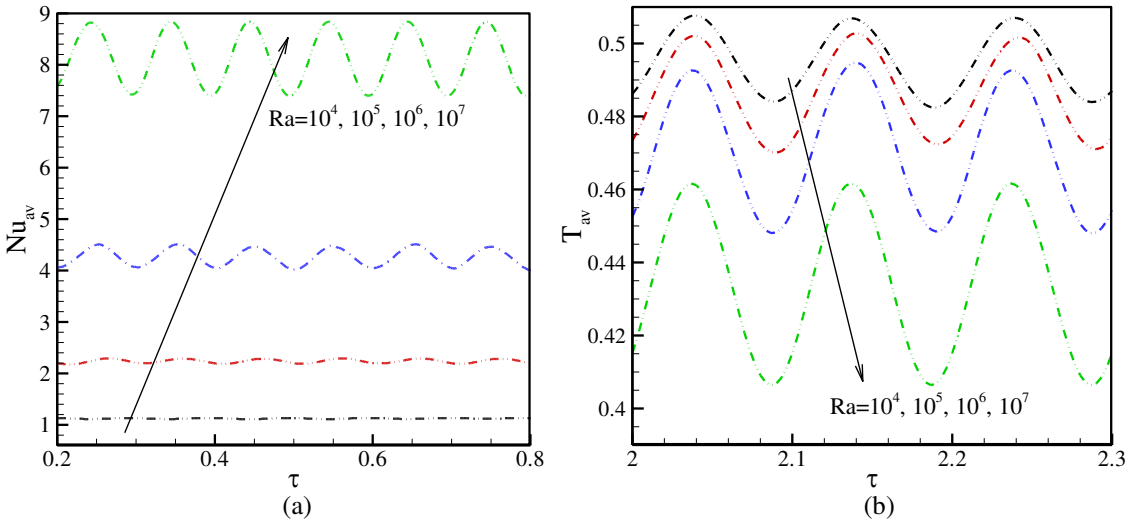

Fig. 9. Average Nusselt number (a) and the average temperature (b) versus dimensionless time for different values of Ra in $f = 10\pi$, $E_\tau = 10^{13}$, and $Pr = 6.2$

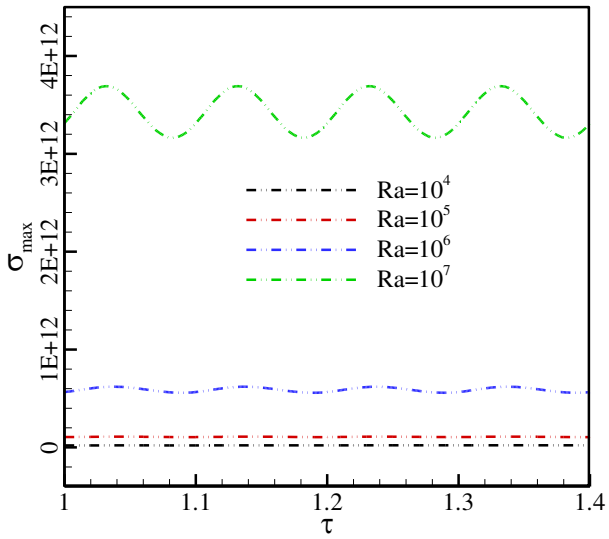

Fig. 10. The maximum stress in the flexible membrane versus dimensionless time for different values of *Ra* in $f=10\pi$, $E_\tau = 10^{13}$, and $Pr = 6.2$

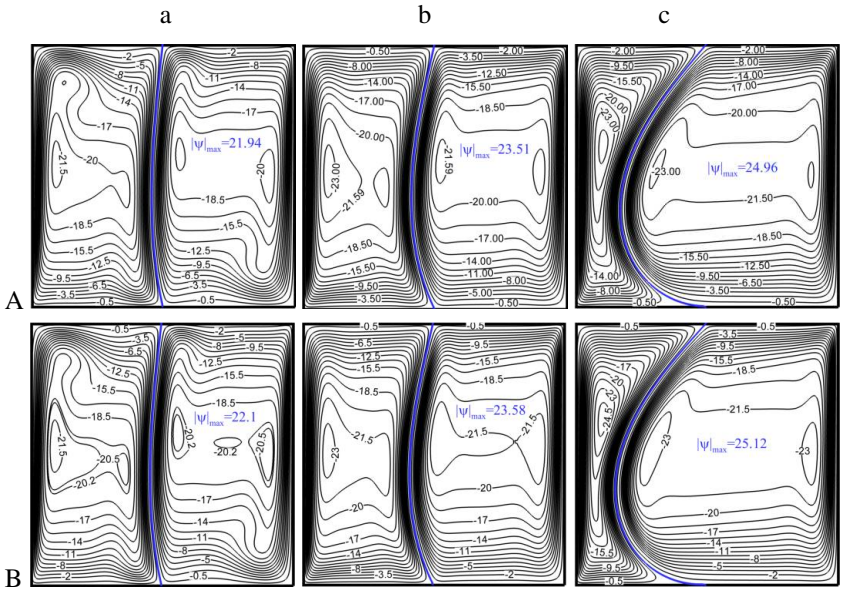

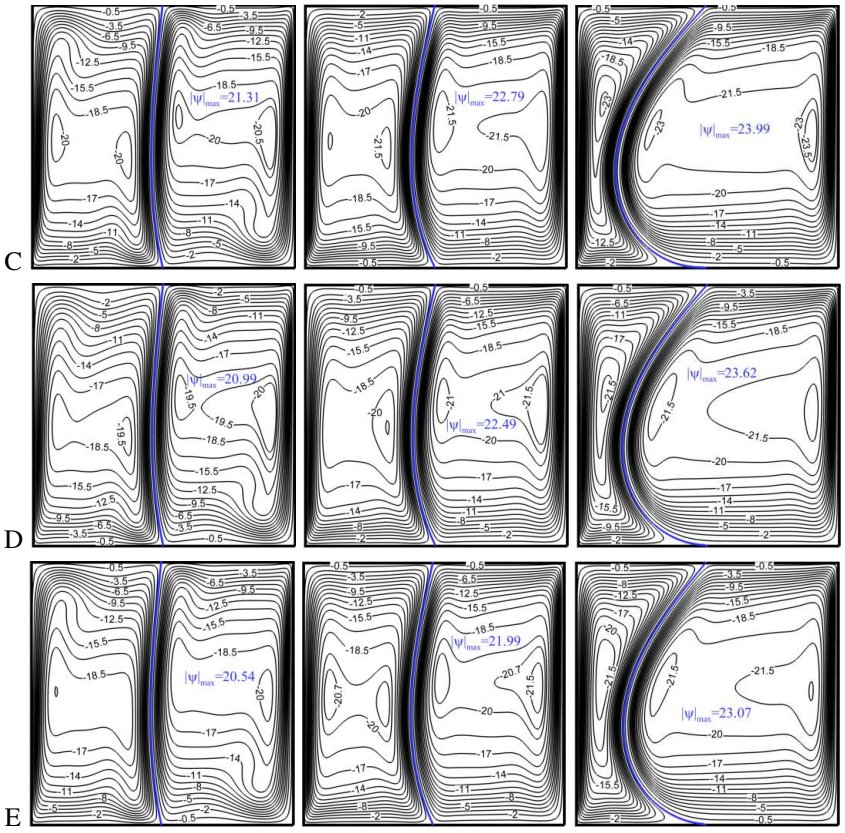

Fig. 11. Streamlines contours for Prandtl number a: Pr = 0.71 b: Pr = 6.2 and c: Pr = 200 in a period of oscillation (A: nT_p, B: nT_p+T_p/5, C: nT_p+$2T_p$/5, D: nT_p+$3T_p$/5, and E: nT_p+$4T_p$/5) for Ra = 10^7, f = 10 π and E_τ = 10^{14}

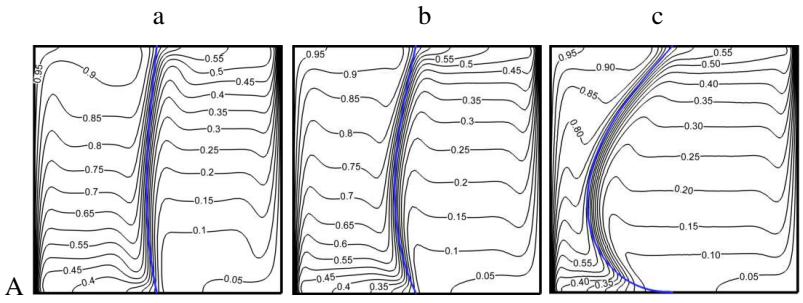

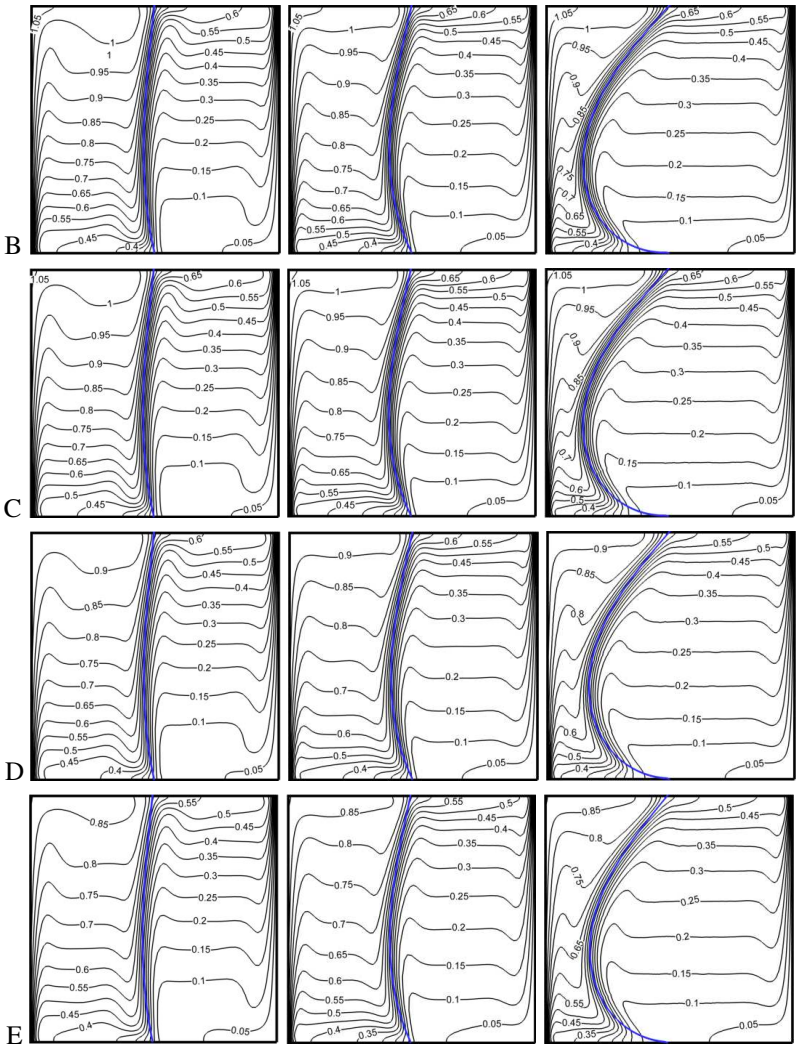

Fig. 12. Isotherm contours for Prandtl number a: Pr = 0.71, b: Pr = 6.2 and c: Pr = 200 in a period of oscillation (A: nT_p, B: nT_p+T_p/5, C: nT_p+2T_p/5, D: nT_p+3T_p/5, E: nT_p+4T_p/5) for $Ra = 10^7$, $f = 10\pi$ and $E_\tau = 10^{14}$

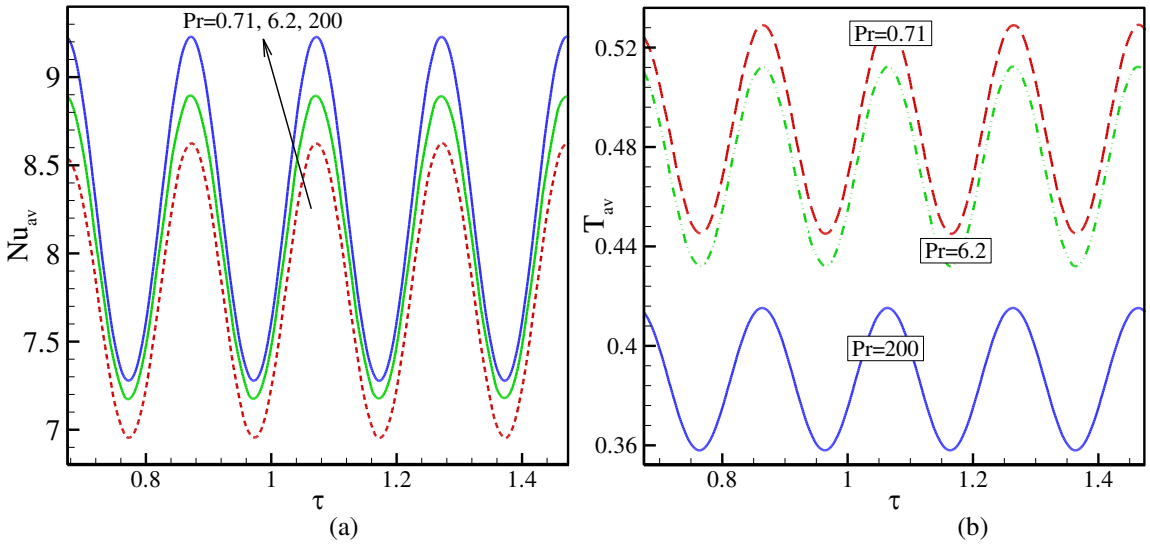

Fig. 13. The average Nusselt number on the right wall (a) and the average temperature inside whole cavity (b) for different periods of oscillation with Prandtl number $Pr = 0.71$, 6.2 and 200 for $Ra = 10^7$, $f = 10\pi$ and $E_\tau = 10^{14}$

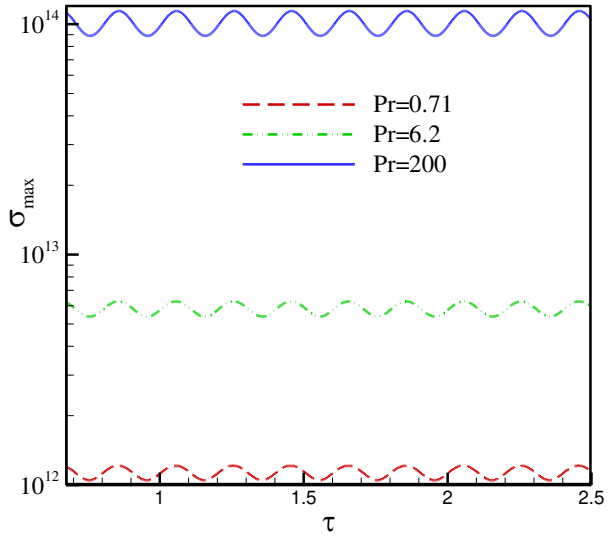

Fig. 14. Maximum stress σ_{max} according to dimensionless time for the different values of Pr in $Ra = 10^7$, $f = 10\pi$ and $E_\tau = 10^{14}$

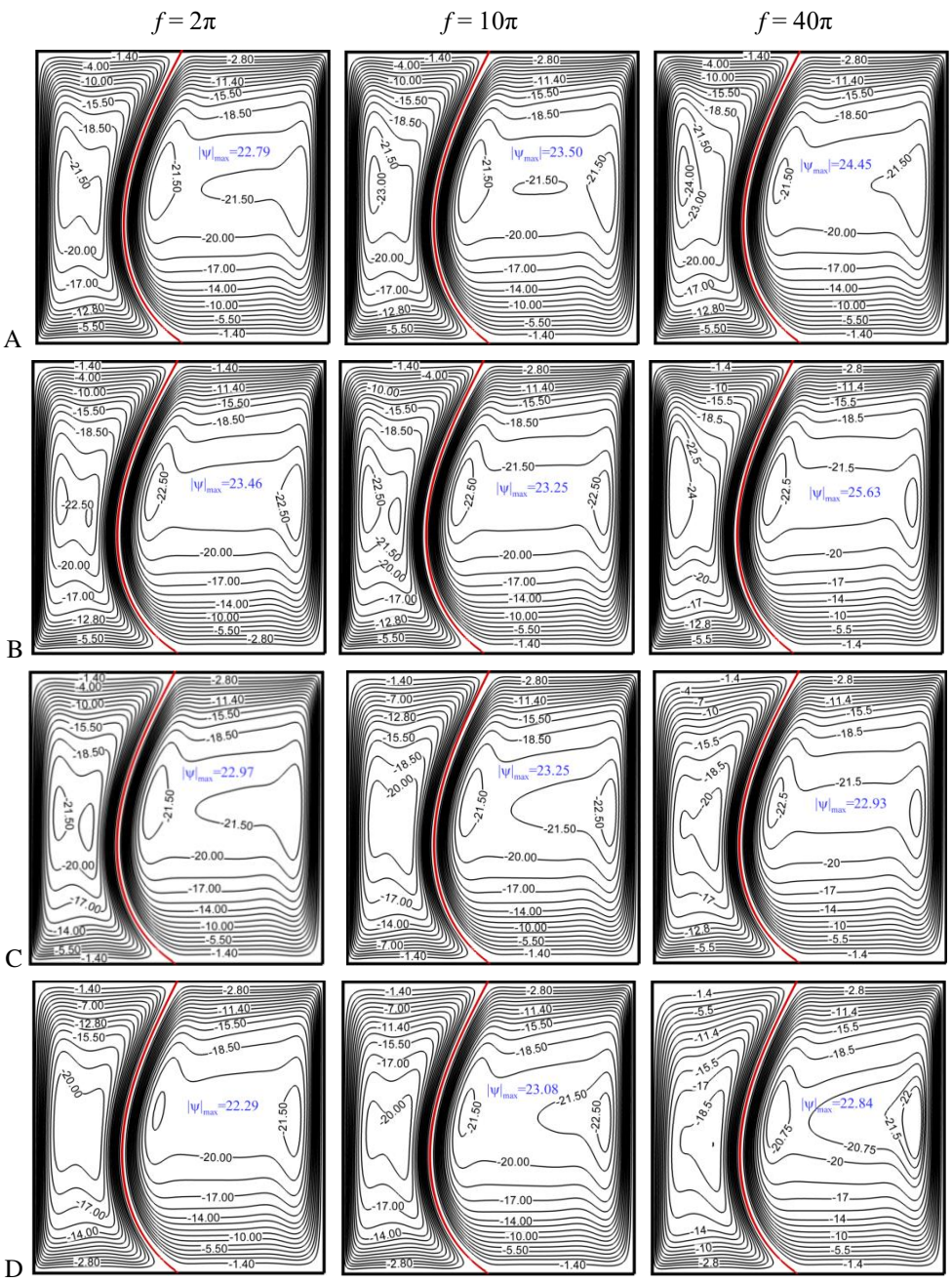

Fig. 15. Streamline contours for the different values of frequency in different periods of oscillation (A: nT_p, B: $nT_p+T_p/4$, C: $nT_p+T_p/2$, D: $nT_p+3T_p/4$) for $Ra = 10^7$, $Pr = 6.2$ and $E_\tau = 10^{14}$

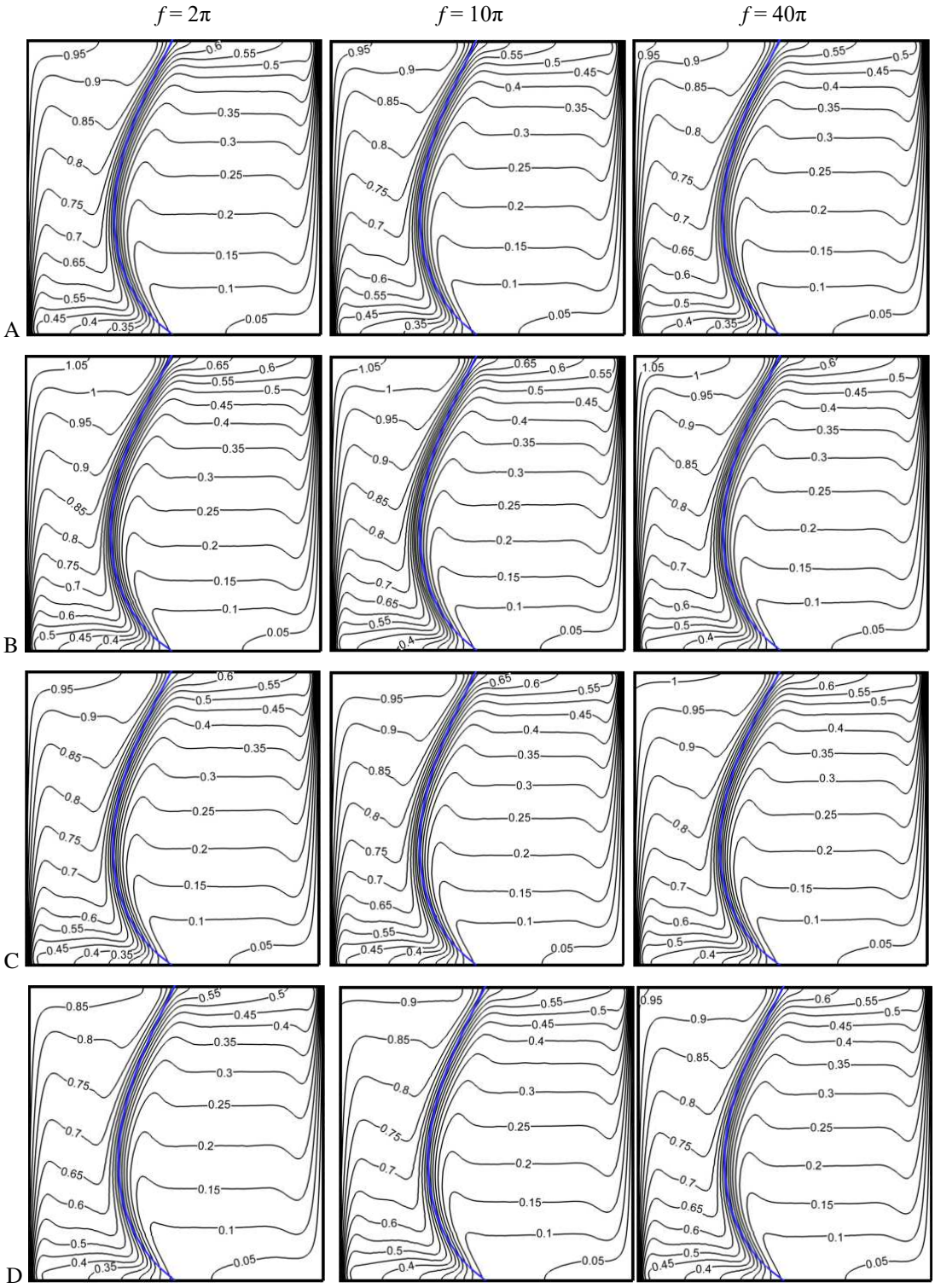

Fig. 16. Isotherms contours for different frequency values and different periods of oscillation (A: nT_p, B: nT_p+T_p/4, C: nT_p+T_p /2, D: nT_p+$3T_p$ /4) for $Ra = 10^7$, $Pr = 6.2$ and $E_\tau = 10^{14}$

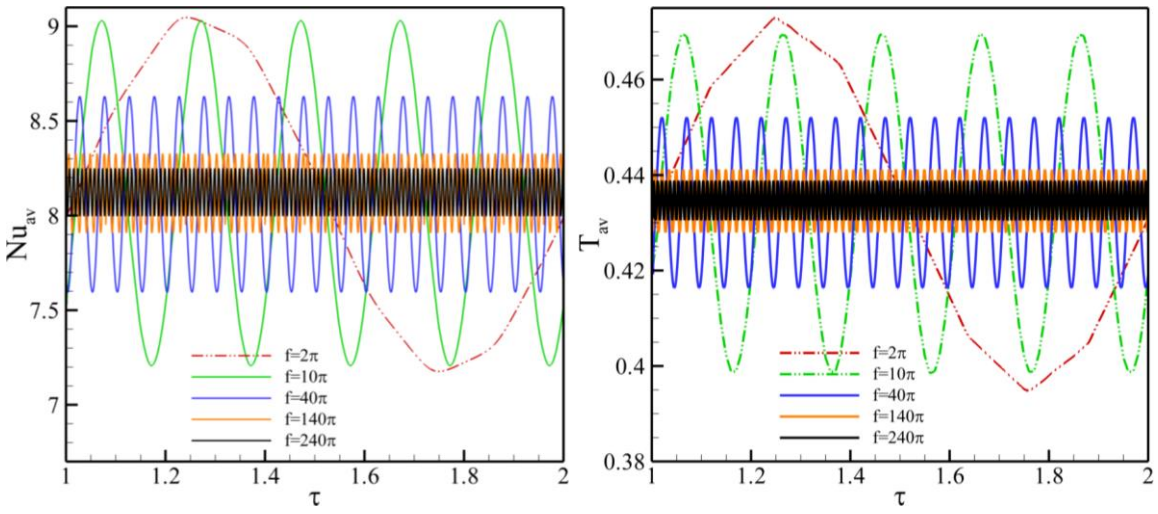

(a) (b)

Fig. 17. Variations of (a): average Nusselt number Nu_{av} and (b) average temperature T_{av} versus dimensionless time for the different values of frequency in Ra=10^7, Pr = 6.2, and E_τ=10^{14}

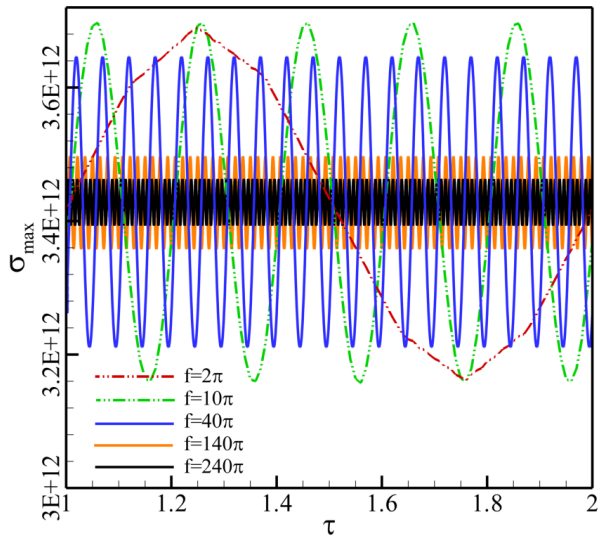

Fig. 18. Variations σ_{max} according to dimensionless time for the different values of frequency in Ra=10^7, Pr = 6.2, and E_τ=10^{14}

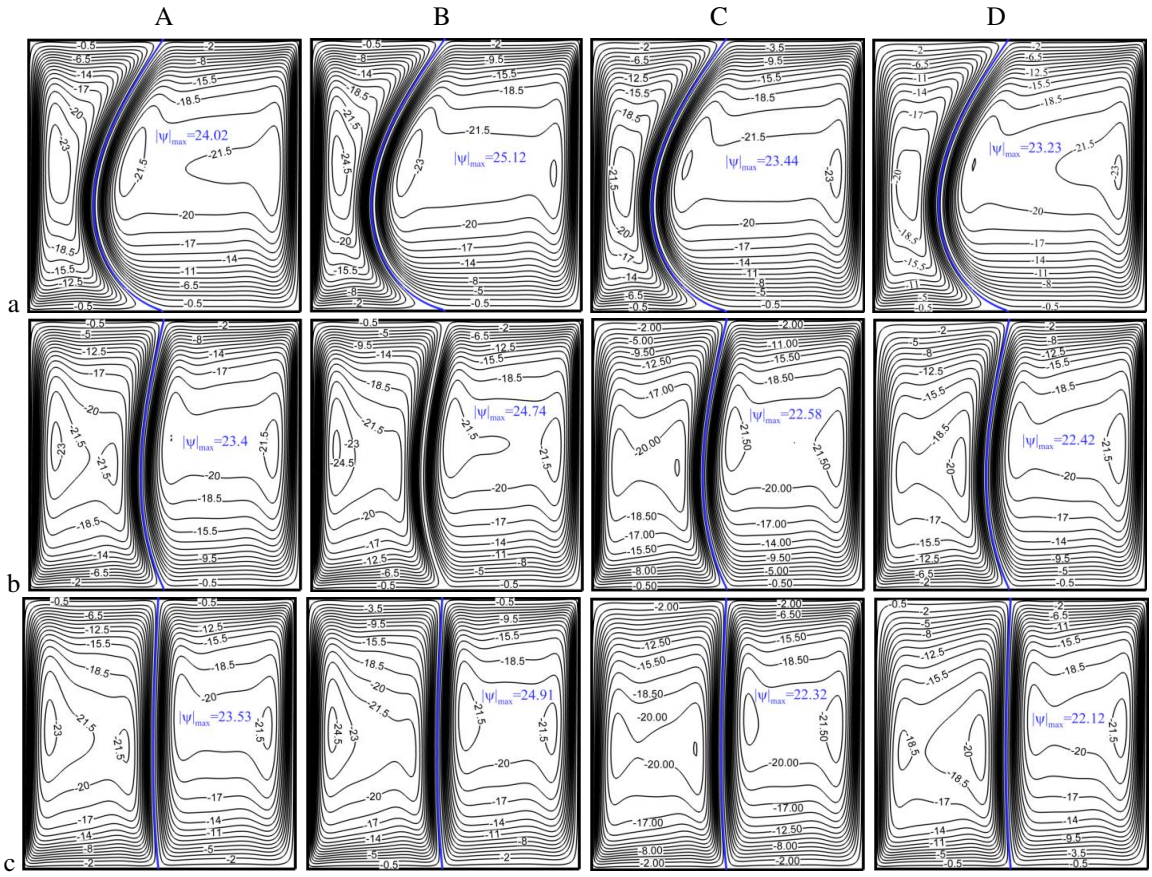

Fig. 19. Streamlines for the cavities with modulus elasticity a: E_τ=5×10^{12}, b: E_τ=10^{14} and c: E_τ=10^{16} in different periods of oscillation (A: nT_p, B: nT_p+T_p/4, C: nT_p+T_p /2, D: nT_p+3T_p /4) for Ra = 10^7, f = 20π and Pr = 6.2

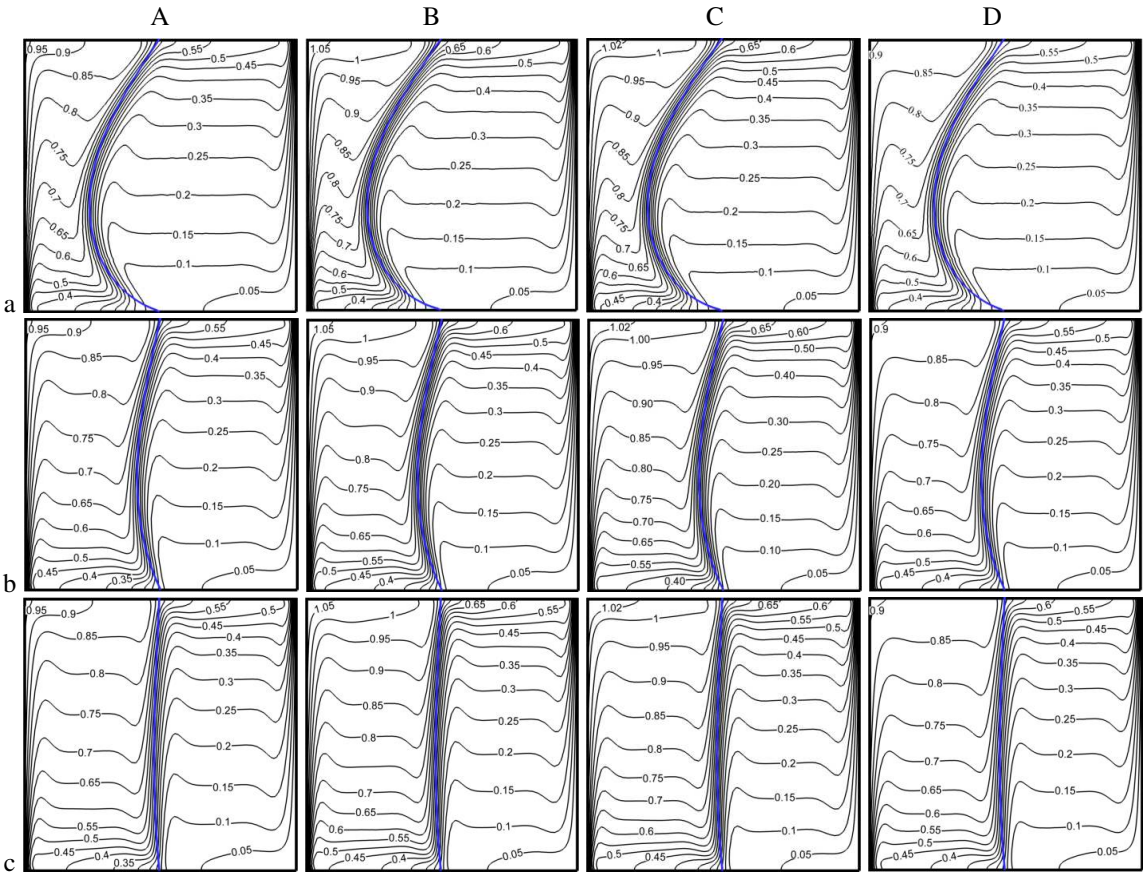

Fig. 20. Isotherms contours for the cavities with modulus elasticity a: E_τ=5×10^{12}, b: E_τ=10^{14} and c: E_τ=10^{16} in different periods of oscillation (A: nT_p, B: nT_p+T_p/4, C: nT_p+T_p /2, D: nT_p+3T_p /4) for Ra = 10^7, f = 20π and Pr = 6.2

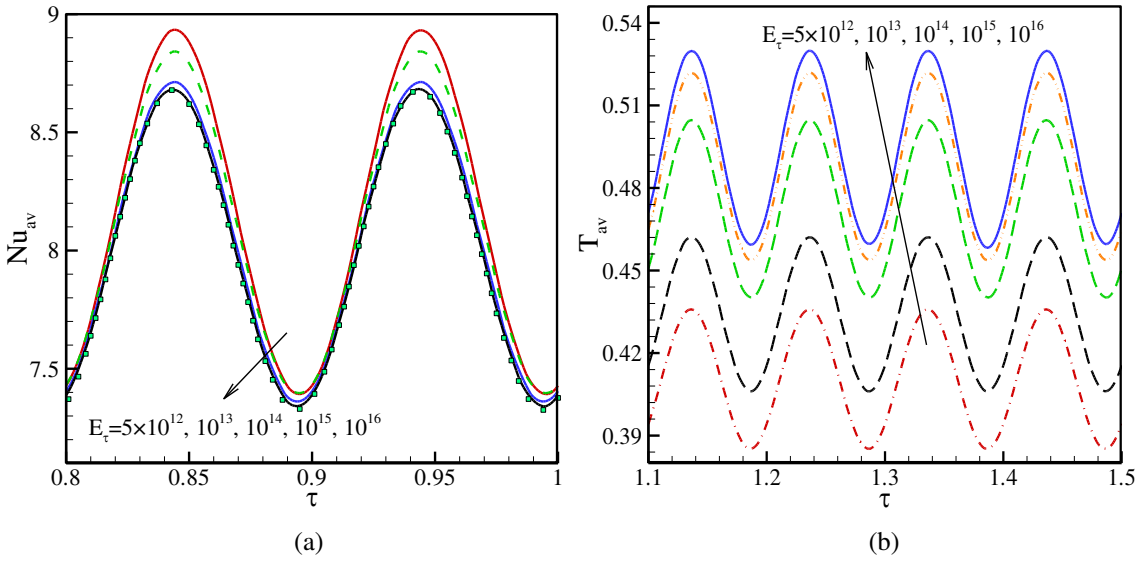

Fig. 21. Variations of Nu_{av} (a) and T_{av} (b) versus oscillation period for different values of E_τ at $Ra = 10^7$, $f = 20\pi$ and $Pr = 6.2$

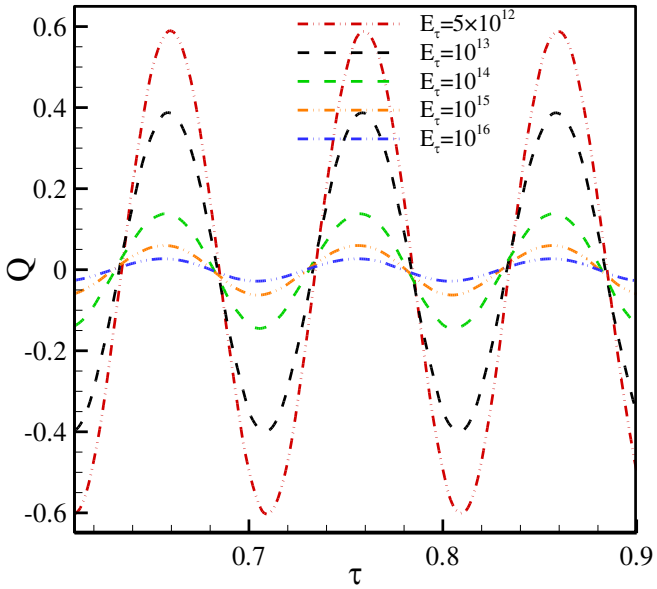

Fig. 22. The dimensionless flow rate through the left embedded eyelet versus oscillation period for different values of E_τ at $Ra = 10^7$, $f = 20\pi$ and $Pr = 6.2$

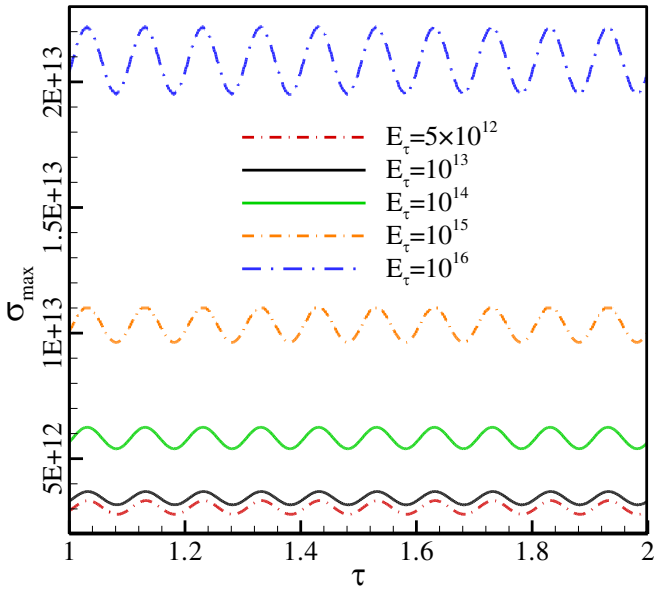

Fig. 23. Variations of σ_{max} versus oscillation period for different values of E_τ at $Ra = 10^7$, $f = 20\pi$ and $Pr = 6.2$